Two-fluid flowing equilibrium configurations of HIST spherical torus plasmas sustained by double pulsing coaxial helicity injection

T. Kanki[1], M. Nagata[2]

[1] *Japan Coast Guard Academy, Kure, Japan*

[2] *University of Hyogo, Himeji, Japan*

Refluxing approach of coaxial helicity injection (CHI) which operates in multi-pulsing CHI (M-CHI) has been proposed [1]. In the M-CHI scenario, current driven (sustainment) phase to perform the CHI by applying the gun voltage and decay phase to obtain the excellent confinement by partially decaying the plasma current and magnetic field are separated in time. To explore the usefulness of the M-CHI for spherical torus (ST) configurations, the double pulsing operations have been tested in the HIST device, verifying the flux amplification and the formation of the closed flux surfaces after the second CHI pulse [2]. The purpose of this study is to investigate characteristics of the magnetic field and plasma flow structures during the sustainment by comparing the results of plasma flow, density, and magnetic fields measurements with those of two-fluid equilibrium calculations.

For two-fluid equilibrium calculations, let us assume axisymmetry about HIST geometric axis (see Fig. 4) in cylindrical coordinates (r, θ, z). Using the dimensionless variables, an axisymmetric two-fluid flowing equilibrium can be described by a pair of generalized Grad-Shafranov equations for ion surface variable Y and electron surface variable ψ [3],

$$\overline{\psi}_i' r^2 \nabla \cdot \left(\frac{\overline{\psi}_i'}{n} \frac{\nabla Y}{r^2} \right) = \frac{r}{\varepsilon} \left(B_\theta \overline{\psi}_i' - n u_\theta \right) + n r^2 \left(H_i' - T_i S_i' \right), \tag{1}$$

$$r^2 \nabla \cdot \left(\frac{\nabla \psi}{r^2} \right) = \frac{r}{\varepsilon} \left(B_\theta \overline{\psi}_e' - n u_\theta \right) - n r^2 \left(H_e' - T_e S_e' \right), \tag{2}$$

and a generalized Bernoulli equations for the number density n,

$$\frac{\gamma}{\gamma - 1} n^{\gamma - 1} \exp\left[(\gamma - 1) S_i \right] + \frac{u^2}{2} + \phi_E = H_i, \tag{3}$$

$$\frac{\gamma}{\gamma - 1} n^{\gamma - 1} \exp\left[(\gamma - 1) S_e \right] - \phi_E = H_e. \tag{4}$$

Here $\boldsymbol{u}$, $\boldsymbol{B}$, T_α, ϕ_E, and γ are the ion flow velocity, magnetic field, temperature of species (α=i, e), electrostatic potential, and adiabatic constant, respectively. Also, the two-fluid parameter ε is defined by the ratio of the ion skin depth $\ell_i = \sqrt{m_i / (\mu_0 n e^2)}$ (m_i and e are ion mass and electron charge, respectively.) to the system length scale R (the radius of the flux conserver (FC) used in the HIST, R=0.5 m), $\varepsilon = \ell_i / R$, and ε=0.0644 is given by using $\ell_i = 3.2$ cm

through $n = 5.0 \times 10^{19}$ m^{-3} observed in the HIST experiment. The value of γ is assumed as 5/3 in the calculation. Note that ψ corresponds to the familiar poloidal flux function. The poloidal flow stream function $\overline{\psi}_\alpha$, total enthalpy function H_α, and entropy function S_α are arbitrary surface functions of their respective surface variables. The three arbitrary functions $\Lambda_\alpha (\equiv \overline{\psi}_\alpha')$, H_α, and S_α for each species can be assumed so as to reflect the current density $\boldsymbol{j}$, $\boldsymbol{B}$, n, and $\boldsymbol{u}$ profiles on the basis of the experimental data by choosing appropriate function forms,

$$\Lambda_\alpha(Y) = \Lambda_{\alpha 0} + (\Lambda_{\alpha 1} - \Lambda_{\alpha 0}) \left. \frac{df}{dx} \right|_{Y-\Delta Y;\delta_{\alpha 0},\delta_{\alpha 1},\delta_{\alpha 2}},$$

$$H_\alpha(\mathrm{Y}) = H_{\alpha 0} + (H_{\alpha 1} - H_{\alpha 0}) \left. \frac{dg}{dx} \right|_{Y-\Delta Y;\delta_{\alpha 1},\delta_{\alpha 2}}, \quad S_\alpha(\mathrm{Y}) = S_{\alpha 0} + (S_{\alpha 1} - S_{\alpha 0}) \left. \frac{dg}{dx} \right|_{Y-\Delta Y;\delta_{\alpha 1},\delta_{\alpha 2}},$$

$$f(x;\delta_0,\delta_1,\delta_2) = \begin{cases} -\dfrac{1}{\delta_0\delta_1}\left[\dfrac{\delta_0^4}{12}\left(1-\dfrac{2\delta_1}{\delta_0}\right) + x^2\left\{\dfrac{\delta_0\delta_1}{2} + x\left(\dfrac{\delta_0+\delta_1}{3}+\dfrac{x}{4}\right)\right\}\right]; & x < 0 \\ -\dfrac{\delta_0^3}{12\delta_1}\left(1-\dfrac{2\delta_1}{\delta_0}\right) - \delta_2\left\{x - \delta_2 \log\left(1+\dfrac{x}{\delta_2}\right)\right\}; & x \geq 0 \end{cases}, \tag{5}$$

$$g(x;\delta_1,\delta_2) = \frac{1}{\delta_1+\delta_2}\begin{cases} \delta_1^2 \exp[x/\delta_1]; & x < 0 \\ \delta_1 x + \delta_2\sqrt{\delta_2^2 + x^2} - \delta_2^2 + \delta_1^2; & x \geq 0 \end{cases}.$$

Here $\Lambda_{\alpha 0}$, $\Lambda_{\alpha 1}$, $H_{\alpha 0}$, $H_{\alpha 1}$, $S_{\alpha 0}$, $S_{\alpha 1}$, $\delta_{\alpha 0}$, $\delta_{\alpha 1}$, $\delta_{\alpha 2}$, and ΔY are constant parameters. Equations (1) and (2) have terms of order $1/\varepsilon$ on the right-hand side, and they cause singularities. We employ the nearby-fluids procedure to eliminate the singularities [3].

Next, we consider the boundary conditions for Eqs. (1)-(4). No magnetic flux penetrates the FC, central conductor, and entrance port of the FC. Therefore, ψ is fixed at 0 at the FC wall and surface of the central conductor and entrance port. The bias flux is given by assigning fixed values of ψ to grid points corresponding to the right open end. These values are calculated using a quadratic function of r. The vacuum toroidal field $B_{t,v}$ is produced by a toroidal field coil current I_{tf} along the geometric axis inside the central conductor. Under the above assumptions and boundary conditions, the equilibrium is numerically determined by using a successive over-relaxation method for updating ψ and a Newton-Raphson method for updating n [4].

On the basis of the above numerical results, we investigate the fundamental characteristics of the magnetic field and plasma flow structures of HIST equilibria obtained in the double pulsing CHI experiments. The radial profiles of $\boldsymbol{B}$ and $\boldsymbol{j}$ structures at the midplane are shown in Fig.1. Due to the steep density gradient, the toroidal field B_t has a diamagnetic profile (high volume average beta value of 68 %) in the central open flux column (OFC) region $(0.06\ \mathrm{m} \leq R \leq 0.13\ \mathrm{m})$. The poloidal field B_z is relatively large and comparable to B_t in the

OFC region. The toroidal current density j_t (total toroidal current I_t of 266 kA) has a maximum value in the OFC region and is almost zero in the outer edge region. The poloidal current density j_z (total poloidal current I_p of 106 kA) is relatively large and comparable to j_t in the OFC region. Parallel current density λ has a maximum value around the separatrix in the inboard side ($R \sim 0.13$ m) and indicates an oscillating profile. All the calculated values of $\boldsymbol{B}$ and $\boldsymbol{j}$ are somewhat larger than the measured values on HIST, but their profiles are consistent with the observations. The radial profiles of n and T_α at the midplane are shown in Fig. 2. The n has a steep gradient scale around the separatrix which is comparable to ℓ_i. The density gradient in high field side of the experiment is much steeper than that of calculation, and is not so steep in outer edge region. Both T_i and T_e have the same profiles which gradually rise towards the periphery region, and their magnitudes are somewhat larger than the observations. The radial profiles of toroidal and poloidal flow velocities at the midplane are shown in Fig. 3. The $\boldsymbol{u}$ with strong flow shear from the separatrix in the inboard side towards the core region is the opposite direction to the electron flow velocity $\boldsymbol{u}_e$ due to the diamagentic drift through the density gradient. Both of I_t and I_p are carried by both $\boldsymbol{u}$ and $\boldsymbol{u}_e$. The electron fluid mostly moves along the magnetic field. The toroidal ion flow velocity u_t is the same direction as I_t except in the inner edge and core region. The poloidal ion flow velocity u_p is the same direction as I_p except in the both edge regions. The maximum values of u_t (~ 35 km/s) and u_p (~ 20 km/s), and their directions are agreement with the observations. Figure 4 shows the poloidal flux contours and safety factor q as a function of the normalized poloidal flux function ψ/ψ_{axis}. Here ψ_{axis} indicates the value of ψ at the magnetic axis. The equilibrium is axially elongated, and the flux quantities are principally concentrated on the periphery region due to the hollow current profile. The q profile shows a reversed shear magnetic configuration with $q > 2$. We investigate the generalized Ohm's law,

$$\boldsymbol{E} + (1/\varepsilon)\boldsymbol{u}\times\boldsymbol{B} + \boldsymbol{F}_{2F} = 0, \quad \boldsymbol{F}_{2F} = -\nabla p_i / n - \boldsymbol{u}\cdot\nabla\boldsymbol{u} = \nabla p_e / n - (\nabla\times\boldsymbol{B})\times\boldsymbol{B}/n. \tag{6}$$

Here $\boldsymbol{E}$, $(1/\varepsilon)\boldsymbol{u}\times\boldsymbol{B}$, and $\boldsymbol{F}_{2F}$ express the electric field, Lorentz force, and two-fluid effects, respectively. The term $-\nabla p_i / n$, $-\boldsymbol{u}\cdot\nabla\boldsymbol{u}$, $\nabla p_e / n$, and $-(\nabla\times\boldsymbol{B})\times\boldsymbol{B}/n$ cause the ion diamagnetic, inertia, electron diamagnetic drifts and Hall effect, respectively. The radial profiles of $\boldsymbol{E}$, $(1/\varepsilon)\boldsymbol{u}\times\boldsymbol{B}$, $\boldsymbol{F}_{2F}$, $-\nabla p_i / n$, $-\boldsymbol{u}\cdot\nabla\boldsymbol{u}$, $\nabla p_e / n$, and $-(\nabla\times\boldsymbol{B})\times\boldsymbol{B}/n$ at the midplane are shown in Fig. 5. All terms are radial components. The $\boldsymbol{E}$ is relatively small, and thus $(1/\varepsilon)\boldsymbol{u}\times\boldsymbol{B}$ nearly balances with $\boldsymbol{F}_{2F}$. The $\boldsymbol{F}_{2F}$ is particularly significant in a region with the steep density gradient due to the ion and electron diamagnetic drifts and Hall effects. The ion inertia effect is relatively small in the whole region.

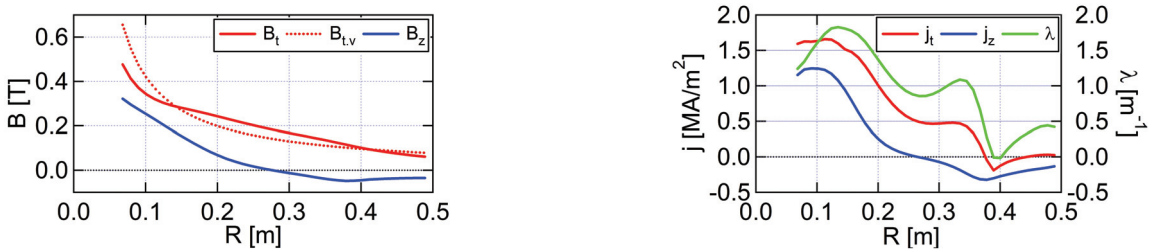

Fig. 1 Radial profiles of the magnetic fields and current densities at the midplane

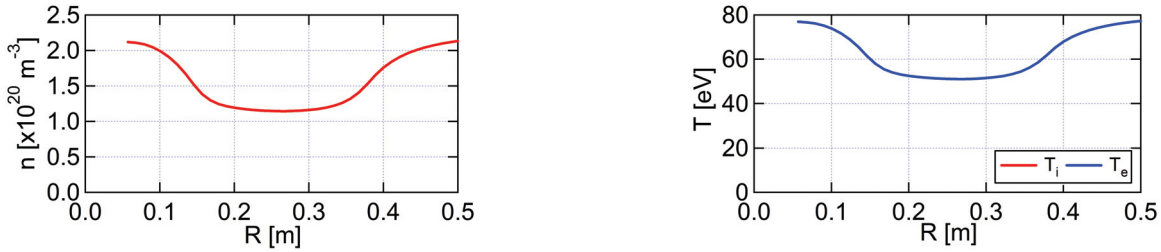

Fig. 2 Radial profiles of the number density and temperatures at the midplane

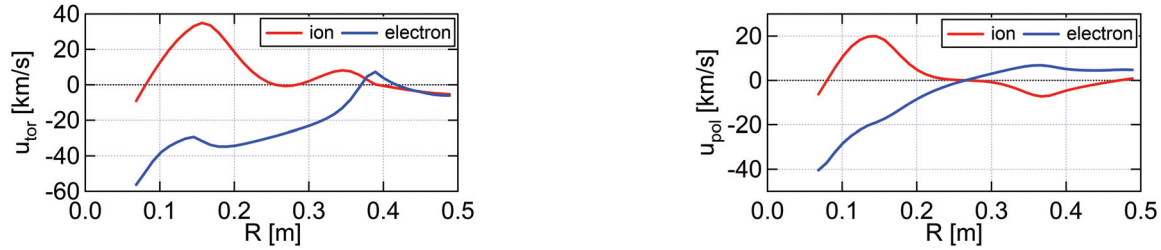

Fig. 3 Radial profiles of the toroidal and poloidal flow velocities at the mideplane

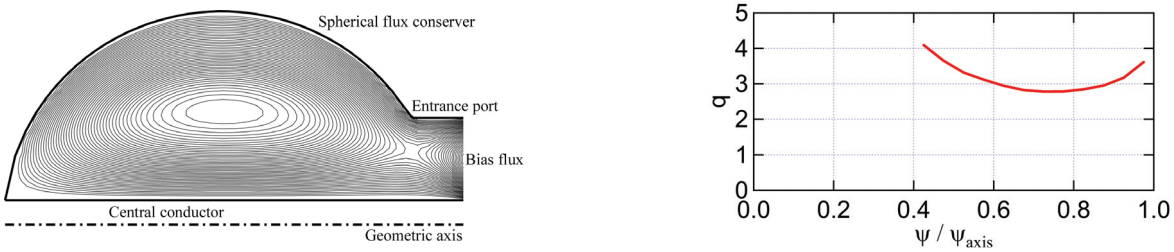

Fig. 4 Poloidal flux contours and safety factor q as a function of the normalized poloidal flux function $\psi/\psi_{\mathrm{axis}}$

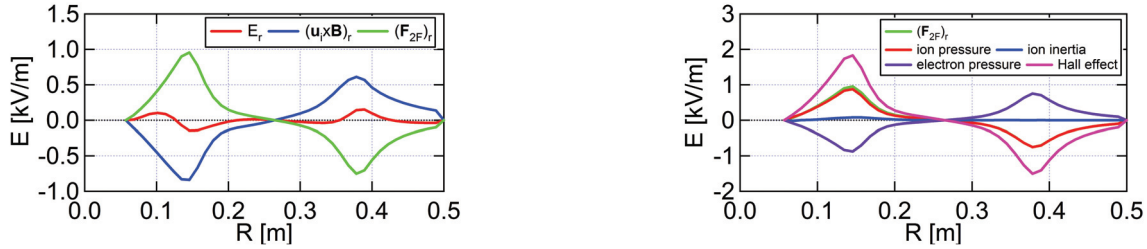

Fig. 5 Radial profiles of $\boldsymbol{E}$, $(1/\varepsilon)\boldsymbol{u}\times\boldsymbol{B}$, $\boldsymbol{F}_{2F}$, $-\nabla p_i/n$, $-\boldsymbol{u}\cdot\nabla\boldsymbol{u}$, $\nabla p_e/n$, and $-(\nabla\times\boldsymbol{B})\times\boldsymbol{B}/n$ at the midplane

References

[1] E.B. Hooper, Plasma Phys. Control. Fusion **53**, 085008 (2011).

[2] M. Nagata *et al.*, *24th IAEA Fusion Energy Conference* (San Diego, USA) ICC/1-1Rb (2012).

[3] L.C. Steinhauer and A. Ishida, Phys. Plasmas **13**, 052513 (2006).

[4] T. Kanki *et al.*, Plasma and Fusion Res. **3**, S1066 (2008).